

Article

Regional Monitoring of Leaf Chlorophyll Content of Summer Maize by Integrating Multi-Source Remote Sensing Data

Hongwei Tian^{1,2}, Lin Cheng^{1,2,*}, Dongli Wu^{3,*}, Qingwei Wei^{1,4} and Liming Zhu⁵ 

¹ Key Laboratory of Agrometeorological Safeguard and Applied Technique, China Meteorological Administration, Zhengzhou 450003, China; thwenigma@163.com (H.T.)

² Institute of Meteorological Sciences of Henan Province, Zhengzhou 450003, China

³ China Meteorological Administration, Atmospheric Observation Center, Beijing 100081, China

⁴ Hebi Meteorological Bureau, Hebi 458030, China

⁵ College of Hydraulic Science and Engineering, Yangzhou University, Yangzhou 225009, China

* Correspondence: rainwood2@163.com (L.C.); wudongli666@126.com (D.W.)

Abstract: This study addresses the problem of restricted ability for large-scale monitoring due to the limited cruising time of unmanned aerial vehicles (UAV) by identifying an optimal leaf Chlorophyll content (LCC) inversion machine learning model at different scales and under different parameterization schemes based on simultaneous observations of ground sampling, UAV flight, and satellite imagery. The following results emerged: (1) The correlation coefficient between most remote sensing features (RSFs) and LCC increased as the remote scale expanded; thus, the scale error caused by the random position difference between GPS and measuring equipment should be considered in field sampling observations. (2) The LCC simulation accuracy of the UAV multi-spectral camera using four machine learning algorithms was ExtraTree > GradientBoost > AdaBoost > RandomForest, and the 20- and 30-pixel scales had better accuracy than the 10-pixel scale, while the accuracy for three feature combination schemes ranked combination of extremely significantly correlated RSFs > combination of significantly correlated and above RSFs > combination of all features. ExtraTree was confirmed as the optimal model with the feature combination of scheme 2 at the 20-pixel scale. (3) Of the Sentinel-2 RSFs, 27 of 28 were extremely significantly correlated with LCC, while original band reflectance was negatively correlated, and VIs were positively correlated. (4) The LCC simulation accuracy of the four machine learning algorithms ranked as ExtraTree > GradientBoost > RandomForest > AdaBoost. In a comparison of two parameterization schemes, scheme 1 had better accuracy, while ExtraTree was the best algorithm, with 11 band reflectance as input RSFs; the RMSE values for the training and testing data sets of 0.7213 and 1.7198, respectively.

Keywords: leaf Chlorophyll content; machine learning; scale transformation; unmanned aerial vehicle remote sensing; Sentinel-2



Citation: Tian, H.; Cheng, L.; Wu, D.; Wei, Q.; Zhu, L. Regional Monitoring of Leaf Chlorophyll Content of Summer Maize by Integrating Multi-Source Remote Sensing Data. *Agronomy* **2023**, *13*, 2040. <https://doi.org/10.3390/agronomy13082040>

Academic Editor: Hesong Wang

Received: 30 May 2023

Revised: 18 July 2023

Accepted: 25 July 2023

Published: 31 July 2023



Copyright: © 2023 by the authors. Licensee MDPI, Basel, Switzerland. This article is an open access article distributed under the terms and conditions of the Creative Commons Attribution (CC BY) license (<https://creativecommons.org/licenses/by/4.0/>).

1. Introduction

Agriculture currently faces a serious challenge: the need to meet increasing demand for agricultural production despite limited soil and water resources due to the increasing population and the rapidly growing economy. Field crops (maize, soybeans, canola, and wheat) have expanded to occupy an increasing proportion of the agricultural landscape worldwide. Agricultural intensification has been associated with soil degradation and excessive nitrogen application, leading to environmental contamination [1,2] and, ultimately, economic losses [3,4]. Maize, one of the most vital food crops, provides at least 30% of food calories together with rice and wheat to more than 4.5 billion people in developing countries [5,6]. Consequently, precision agriculture has emerged as a farming management strategy that takes temporal and spatial variability into account with the goal of improving the sustainability of agricultural production. Collecting, processing, and analyzing multi-source data yield information is vital to a decision support system concerning irrigation,

fertilization, and spraying that can be applied at the right place, right time, and right quantity [7].

Leaf Chlorophyll content (LCC), a key biophysical parameter for crop monitoring, signals the ability of a plant to conduct material and energy exchange with the external environment and provides clues to growth status, primary productivity, carbon sequestration ability, and nitrogen utilization efficiency, along with other useful information. Conventional methods for estimating Chlorophyll contents include ultraviolet and visible spectrophotometry and fluorescence analysis [8,9], which are time-consuming, labor-intensive, and destructive to crop leaves. Therefore, some scholars proposed the soil and plant analysis development (SPAD) method for nondestructive rapid measurements of the LCC values of leaves by means of light and electricity [10,11]; furthermore, the relative contents of Chlorophyll obtained by Soil and Plant Analyzer Development 502 (SPAD 502) are highly consistent with the results obtained by chemical experiments, supporting the idea of using this approach instead of the traditional chemical measurement method [12]. However, the drawbacks of this method include limited measuring points and unsuitability for measurement involving a large area [13,14].

In recent years, the rapid advancement of satellite remote sensing technology has supported ongoing improvement in the spatial and temporal resolution of remote sensing images, bringing new opportunities for monitoring vegetation physiological parameters at different scales [15,16]. However, low spatial resolution and frequent cloud cover leads to spatial inconsistency between the satellite remote sensing and field data [17]. The introduction of unmanned aerial vehicles (UAVs) was intended to fill the gaps between the ground measurement and satellite remote sensing data by providing centimeter-level spatial resolution and flexible temporal resolution on the landscape scale [18,19]. Specifically, a UAV platform equipped with visible light imaging sensors, spectral sensors, infrared thermal sensors, fluorescence sensors, LIDAR, and other types of sensors could be used to monitor plant height, LAI, biomass, and other physiological traits of crops at the farm scale with high temporal-spatial resolution during adequate weather conditions.

Generally, crop growth parameter retrieval approaches can be classified into three methodological categories: empirical methods, physical model inversion methods, and hybrid regression methods. The physical model considers more factors and complex physical procedures than the other two methods, making it suitable for vegetation parameter inversions in different regions, for different crops, and at different scales; however, this approach is relatively complex and difficult to use [20–22]. In contrast, empirical methods establish a statistical relationship between vegetation indices and the physiological parameters of vegetation, offering high computational efficiency and accurate estimates of vegetation-related physiological parameters [23,24]. Representing a relatively recent branch of empirical methods, machine learning algorithms, such as support vector regression (SVR), back-propagation neural networks (BPNNs), Gaussian process regression (GPR) algorithms, random forest algorithms (RF), and deep neural networks (DNN), are widely used in crop growth status monitoring because of their excellent computing efficiency [25–29].

LCC remote sensing monitoring has included collecting multi-spectral data from UAV, referring to satellites such as the Chinese GaoFen series, the American Landsat series, and the European Sentinel series that have been employed in previous investigations around the globe [30–33]. Methods of inversion have included the regression of vegetation index (VI) or a combination of VIs, machine learning regression, lookup-table (LUT)-based inversion, hybrid regression, etc. That said, most studies have simulated LCC based on UAV or satellite data alone due to the spatial resolution gap between UAV and satellite data. Therefore, further study is still needed to examine the potential use of combined inversion methods based on data at different resolutions for regional LCC monitoring. Zhang et al. integrated UAV and Sentinel-2A data by correcting the satellite reflection with the corresponding UAV band reflection and applied corrected data to an inversion model based on UAV in implementing a method to achieve regional LCC monitoring using Sentinel-2A [30]. Some bands need to be discarded in the correction and model establishment due

to a wave band setting discrepancy between the UAV's multi-spectral camera and the satellite. In the modeling procedure, it is rarely considered that the uncertainty of the relative position and distance between coordinates labeled by GPS and the actual sampling position could induce obvious random deviation.

The purpose of this study was to find a procedure for regional LCC monitoring by integrating UAV and Sentinel satellite data to support governmental agricultural decision making. The specific study objectives were to (1) find the best scale of UAV multi-spectral imagery in the inversion of LCC by comparing the correlation between LCC and remote sensing characteristics, as well as the accuracy of the UAV-monitored LCC result; (2) find the optimal algorithm for the machine learning regressor for LCC inversion based on UAV and Sentinel-2 multi-spectral imagery; (3) integrate UAV and Sentinel-2 multi-spectral data by resizing the high spatial resolution result of LCC from UAV to Sentinel-2 and use it to train Sentinel-2 data, and ultimately expand the LCC inversion from the field scale to the regional scale.

2. Data Sets and Methodology

2.1. Study Area

The experimental field in this study is located in Xun County, Hebi City, Henan Province, China. Two experimental quadrats in summer maize field each having an area of $1 \text{ km} \times 1 \text{ km}$ were selected; the center latitude and longitude of the quadrats were $35^{\circ}32'16'' \text{ N}$, $114^{\circ}16'51'' \text{ E}$ and $35^{\circ}34'23'' \text{ N}$ and $114^{\circ}23'5'' \text{ E}$ (Figure 1).

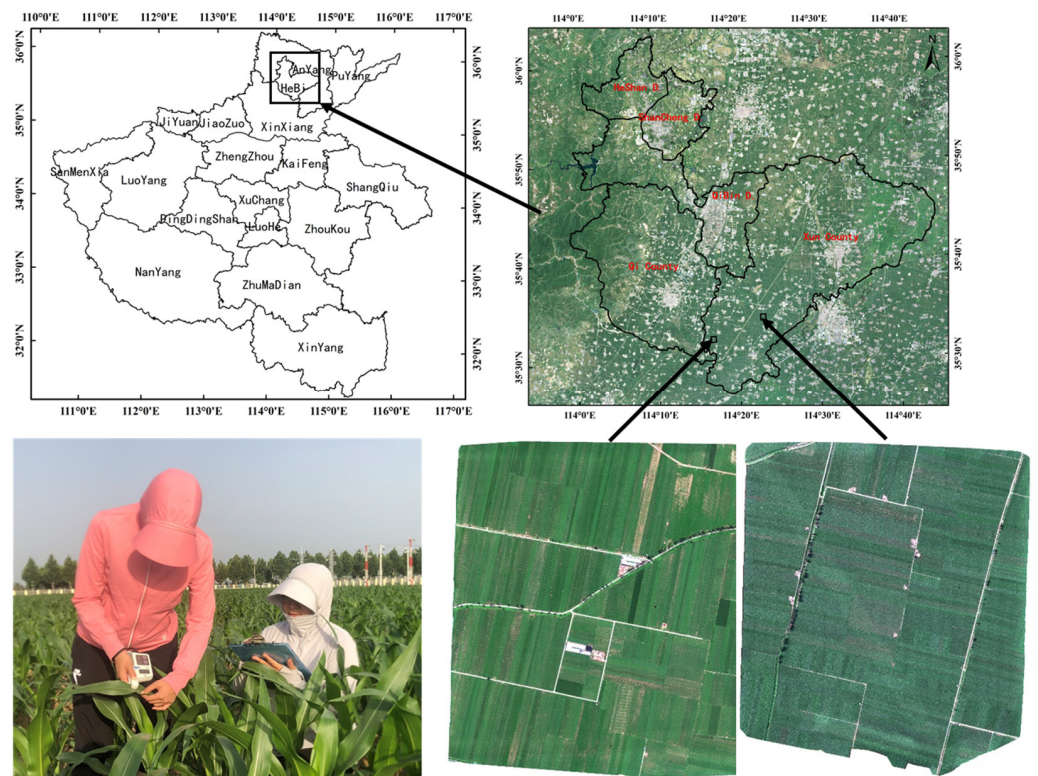


Figure 1. Schematic diagram of geographical location and remote sensing image of the experimental area.

2.2. Data Acquisition

In this study, two field observation experiments were carried out, taking place on 21 July and 31 August 2022, which corresponded to the jointing stage and heading stage of summer maize, respectively. In each quadrat of $1 \text{ km} \times 1 \text{ km}$, the SPAD-502 Plus (Konica-Minolta, Osaka, Japan) Chlorophyll meter was used to randomly sample. Five leaves were measured at each sampling point, and the average value was taken as the LCC value of

the sampling point and recorded, along with the latitude and longitude information of the sampling point. A total of 75 valid sampling data were obtained in the two experiments.

The study adopted a simultaneous flight observation platform of a low-altitude UAV, the DJI Matrice 300 RTK UAV (SZ DJI Technology Co., Ltd., Shenzhen, China), which had a maximum endurance of 55 min and a maximum load of 2.7 kg. The UAV was equipped with a RedEdge multi-spectral camera (MicaSense Inc., Seattle, DC, USA) having five bands: blue (475 nm), green (560 nm), red (668 nm), near infrared (840 nm), and red-edge (717 nm) (Figure 2). The camera had a focal length of 5.5 mm, a field of view angle of 47.2°, and an image resolution of 1280. Flight observation was carried out between Beijing time 10:00 and 15:00. The flying height was set at 100 m (ground resolution was 6 cm) at a speed of 8 m/s, and the navigation and lateral overlap rate were 75%. After the flight operation was completed, the images were spliced and then preprocessed to obtain multi-spectral orthophoto images.



Figure 2. Matrice 300 RTK UAV and RedEdge multi-spectral camera.

The high-resolution earth observation satellite selected Sentinel-2 data consisting of 12 bands with a resolution of 10 m~60 m. The images were acquired on 1 July, 21 July, 5 August, and 4 September 2022. LCC inversion modeling was based on the data from 21 July, the same date on which the first field experiment was carried out. The data were downloaded from the European Space Agency website (<https://scihub.copernicus.eu/s2#home> (accessed on 16 October 2022)). The downloaded file, which was at the L2A level, had been preprocessed with radiometric calibration, orthorectification, and atmospheric correction. In this study, officially recommended SNAP (v8.0) software by the European Space Agency was used to resample all bands of the image to 10 m spatial resolution.

The land use/land cover data for Hebi City adopted the data from Sentinel-2's 10 m resolution land use/land cover time series data set in 2021 (download address: <https://www.arcgis.com/home/item.html> (accessed on 2 July 2022)). The map uses the deep learning artificial intelligence land classification model jointly developed by ESRI, Impact Observatory, and Microsoft, which generates more than 400,000 earth observation data annually by using massive training data sets containing billions of human marker image pixels [34].

2.3. Remote Sensing Feature Selection

The vegetation information in remote sensing images is mainly reflected by the spectral characteristics of green plant leaves and the vegetation canopy, along with their differences and changes. VI is the extraction of spectral information of specific optical parameters of plants, providing rapid, effective qualitative and quantitative analysis of the growth status

of surface crops while enhancing the contrast between crops and interference information, such as soil, atmosphere, illumination, and field of view, which allows the quick reflecting of the growth vitality and coverage status of crops. At present, hundreds of VIs are used worldwide. This study selected 15 commonly used VIs (Table 1), combining them with the reflectance of the multi-spectral camera and Sentinel-2 in each band as the features of remote sensing images.

Table 1. List of VIs Used in the Study.

Vegetation Index	Formula	Reference
Difference Environmental Vegetation Index (DVI)	$DVI = NIR - R$	[35]
Enhanced Vegetation Index (EVI)	$2.5 \times (NIR - RED) / (NIR + 6.0 \times RED - 7.5 \times BLUE + 1)$	[36]
Green Passage Vegetation Index (GNDVI)	$(NIR - Green) / (NIR + Green)$	[35]
Green Chlorophyll Index (GCI)	$NIR / GREEN - 1$	[37]
Modified Normalized Vegetation Index (MNLI)	$(1.5 \times (NIR^2 - Red)) / (NIR^2 + Red + 0.5)$	[38]
Modified Soil-Adjusted Vegetation Index (MSAVI)	$0.5 \times [2 \times NIR + 1 - ((2 \times NIR + 1)^2 - 8 \times (NIR - R))^{0.5}]$	[39]
Modified Simple Ratio (MSR)	$(NIR / Red - 1) / (NIR / Red)^{0.5} + 1$	[38]
Modified Triangular Vegetation Index (MTVI)	$1.5 \times [1.2 \times (NIR - GREEN) - 2.5(RED - GREEN)] / \{[(2 \times NIR + 1)^2 - (6 \times NIR - 5 \times RED^{0.5})]^{0.5} - 0.5\}$	[37]
Normalized Difference Vegetation Index (NDVI)	$NDVI = (NIR - R) / (NIR + R)$	[39]
Nonlinear Vegetation Index (NLI)	$(NIR^2 - Red) / (NIR^2 + Red)$	[35]
Optimizing Soil to Regulate Vegetation Index (OSAVI)	$(NIR - Red) / (NIR + Red + 0.16)$	[35]
Renormalized Vegetation Index (RDVI)	$(NIR - Red) / (NIR + Red)^{0.5}$	[35]
Red-Edge Chlorophyll Index (RECI)	$NIR / RE - 1$	[37]
Ratio Vegetation Index (RVI)	$RVI = NIR / R$	[35]
Soil-Regulated Vegetation Index (SAVI)	$SAVI = ((NIR - R) / (NIR + R + L)) / (1 + L)$	[36]

Note: 1 in SAVI is 0.5.

2.4. Selection of Machine Learning Methods

Scikit-learn is a free machine learning library in Python that provides various commonly used classification, regression, and clustering algorithms, including support vector machine (SVM), Random Forest (RF), Gradient Boosting (GB), K-Means, AdaBoost (AB), Extra Tree (ET), and so on [40]. This study adopted four regression algorithms—AB, ET, GB, and RF to study their simulation accuracy with different combination schemes of UAV multi-spectral camera and Sentinel-2 parameters.

The core principle of AB is to fit a sequence of weak learners (i.e., models that are only slightly better than random guessing, such as small decision trees) on repeatedly modified versions of the data. The predictions from all of the trees are then combined through a weighted majority vote (or sum) to produce the final prediction [41].

ET (extremely randomized trees) essentially consists of randomizing strongly both attribute and cut-point choice while splitting a tree node. In the extreme case, it builds totally randomized trees whose structures are independent of the output values of the learning sample. The strength of the randomization can be tuned to problem specifics by the appropriate choice of a parameter [42].

In GB, a general gradient descent “boosting” paradigm is developed for additive expansions based on any fitting criterion. Specific algorithms are presented for least squares, least absolute deviation, and Huber-M loss functions for regression, along with multiclass logistic likelihood for classification. Special enhancements are derived for the particular case where the individual additive components are regression trees, and tools for interpreting such “TreeBoost” models are presented. GB of regression trees produces competitive, highly robust, interpretable procedures for both regression and classification, especially appropriate for mining less than clean data [43].

RF is a combination of tree predictors such that each tree depends on the values of a random vector sampled independently and with the same distribution for all trees in the forest. The generalization error for forests converges to a limit as the number of trees in the forest becomes large. The generalization error of a forest of tree classifiers depends on

the strength of the individual trees in the forest and the correlation between them. Using a random selection of features to split each node yields error rates that compare favorably to AB but are more robust with respect to noise. Internal estimates, which monitor error, strength, and correlation, are used to determine the response to increasing the number of features used in the splitting. Internal estimates are also used to measure variable importance. These ideas are also applicable to regression [44].

The optimal simulation model and its parameter combination scheme was selected based on the correlation coefficient (R, in Equation (1)) by Pearson correlation analysis and the root mean square error (RMSE, Equation (2)) between the simulated results and observed LCC values of the training data set and test data set:

$$R = \frac{\sum_{i=1}^n (x_i - \bar{x})(y_i - \bar{y})}{\sqrt{\sum_{i=1}^n (x_i - \bar{x})^2} \sqrt{\sum_{i=1}^n (y_i - \bar{y})^2}} \quad (1)$$

$$RMSE = \sqrt{\frac{1}{n} \sum_{i=1}^n (x_i - y_i)^2} \quad (2)$$

where y_i and x_i are the i th observed and predicted LCC values, respectively; \bar{x} and \bar{y} are the mean of the observed and predicted LCC values, respectively; n is the number of the samples.

3. Results

3.1. Correlation Analysis between UAV Remote Sensing Features (RSF) and LCC

The ground resolution of the UAV image was 6cm, but the actual sampling position of latitude and longitude recorded by handheld GPS was random in terms of position and distance. In order to reduce the error caused by this randomness, we took the pixel of latitude and longitude as the center, set the region of interest extending to 10, 20, and 30 pixels in four directions, extracted the mean value of spectral reflectance and VIs in the region of interest, and analyzed the correlation between five bands' reflectance and the 15 VIs and LCC at different spatial scales. The results are presented in Table 2.

Table 2. Correlation Coefficient between UAV Remote Sensing Features and LCC.

RSF	10 Pixels	20 Pixels	30 Pixels	RSF	10 Pixels	20 Pixels	30 Pixels
Blue	−0.5747 **	−0.6138 **	−0.6184 **	MSAVI	−0.2962 *	−0.3895 **	−0.4318 **
Green	−0.8462 **	−0.8605 **	−0.8629 **	MSR	−0.0075	−0.0147	−0.0427
Red	−0.4026 **	−0.4377 **	−0.4324 **	MTVI	−0.3160 **	−0.4051 **	−0.4431 **
NIR	−0.4742 **	−0.5839 **	−0.6240 **	NDVI	0.1342	0.1287	0.1069
Red-edge	−0.8710 **	−0.8832 **	−0.8845 **	NLI	−0.0232	−0.0788	−0.1110
DVI	−0.4188 **	−0.5256 **	−0.5668 **	OSAVI	−0.1703	−0.2534 *	−0.2892 *
EVI	−0.3615 **	−0.4074 **	−0.4985 **	RDVI	−0.3067 **	−0.4090 **	−0.4486 **
GCI	0.6444 **	0.6623 **	0.6624 **	RECI	0.7406 **	0.7597 **	0.7612 **
GNDVI	0.6584 **	0.6911 **	0.6857 **	RVI	−0.0582	−0.0618	−0.0900
MNLI	−0.3754 **	−0.4758 **	−0.5174 **	SAVI	−0.3087 **	−0.4131 **	−0.4534 **

Note: Blue, Green, Red, NIR (Near InfraRed) and Red-edge represent the reflectance of 5 bands: blue, green, red, near infrared, and red-edge, respectively; ** stands for $p < 0.01$; * stands for $p < 0.05$.

Correlation analysis revealed that at the 10-pixel scale, the correlation between MSR, NDVI, NLI, OSAVI, RVI, and LCC failed to pass the significance test, while MSAVI was significantly correlated with LCC and the other 14 RSFs were correlated with LCC at an extremely significant level. At scales of 20 and 30 pixels, the correlation between MSR, NDVI, NLI, RVI, and LCC failed to pass the significance test, while OSAVI was significantly correlated with LCC, and the other 15 RSFs were correlated with LCC at an extremely significant level. At all scales, GCI, GNDVI, NDVI, and RECI were positively correlated with LCC, while other RSFs were negatively correlated with LCC. Comparing the R of the same RSF at different scales, the correlation of most features increased as the scale

expanded. Red and GNDVI had the highest correlation at the middle scale; in contrast, NDVI was the only feature whose correlation coefficient decreased with the scale expansion. Thus, it can be seen that the scale error caused by the random position difference between GPS and measuring equipment should be considered in field sampling observations.

3.2. Optimal Model of UAV Multi-Spectral LCC Inversion

At scales of 10, 20, and 30 pixels, four machine learning algorithms were simulated separately with three RSF combination schemes—a combination of extremely significantly correlated RSFs (expressed as scheme 1), significantly correlated and above RSFs (expressed as scheme 2), all features (expressed as scheme 3)—as the input independent variables of the machine learning model, with 85% of the data as the training set and 15% as the test set. The R and RMSE of different schemes at different scales are displayed in Table 3.

Table 3. Summary of LCC simulation accuracy with UAV multi-spectral.

Regression Algorithm	Accuracy Factor	10 Pixels			20 Pixels			30 Pixels		
		Scheme 1	Scheme 2	Scheme 3	Scheme 1	Scheme 2	Scheme 3	Scheme 1	Scheme 2	Scheme 3
AB	Training R	0.9738	0.9691	0.9678	0.9783	0.9790	0.9822	0.9778	0.9784	0.9816
	Training RMSE	1.6743	1.7960	1.8371	1.5148	1.5040	1.4073	1.5292	1.5144	1.4324
	Test R	0.8723	0.8812	0.8901	0.9487	0.9356	0.8925	0.9519	0.9387	0.9180
	Test RMSE	4.2625	4.1582	3.5127	3.0385	3.1298	3.4663	2.7920	3.0617	3.0771
ET	Training R	1.0000	1.0000	1.0000	1.0000	1.0000	1.0000	1.0000	1.0000	1.0000
	Training RMSE	0.0000	0.0000	0.0000	0.0000	0.0000	0.0000	0.0000	0.0000	0.0000
	Test R	0.9126	0.9022	0.8733	0.9265	0.9419	0.9015	0.9323	0.9316	0.9118
	Test RMSE	3.6804	3.8452	3.7336	3.3194	3.0968	3.3948	3.1503	3.1986	3.1842
GB	Training R	0.9997	0.9997	0.9995	0.9995	0.9996	0.9997	0.9995	0.9995	0.9996
	Training RMSE	0.1897	0.1897	0.2468	0.2286	0.2024	0.1884	0.2385	0.2379	0.2209
	Test R	0.9145	0.9095	0.9140	0.9220	0.9183	0.8796	0.9370	0.9321	0.9017
	Test RMSE	3.7272	3.7791	3.3886	3.2881	3.4188	3.7249	3.0342	3.0801	3.2882
RF	Training R	0.9200	0.9199	0.9130	0.9301	0.9301	0.9365	0.9305	0.9308	0.9359
	Training RMSE	2.8651	2.8689	2.9984	2.6893	2.6868	2.6029	2.6838	2.6762	2.6157
	Test R	0.9158	0.9186	0.8945	0.9403	0.9400	0.9018	0.9442	0.9464	0.9091
	Test RMSE	3.7898	3.7503	3.5754	3.0764	3.0821	3.2973	3.0700	3.0139	3.2076

Note: AB, ET, GB, and RF stand for Adaboost, ExtraTree, GradientBoosting, and Random Forest, respectively.

The results listed in Table 3 reveal that the simulation accuracy of different machine learning models was $ET > GB > AB > RF$. For the training and test data sets at different scales and under different feature combination schemes, the average R of the ET model equaled 1.0 and 0.9149, and the RMSE values were 0.0 and 3.4004, respectively. The average R values of the GB model for the training and test data sets were 0.9996 and 0.9143, respectively, while the RMSE values were 0.2159 and 3.4143, respectively. The R values of the AB model for the training and test data sets were 0.9764 and 0.9143, respectively, while RMSE values were 1.5788 and 3.3887, respectively. The correlation coefficients of the RF model for the training and test data sets were 0.9274 and 0.9234, respectively, while the RMSE values were 2.7430 and 3.3181, respectively.

In the comparison of simulation accuracy at different scales with different feature combination schemes and machine learning models, the accuracy at 20 pixels and 30 pixels was very close, while the simulation accuracy at 10 pixels was relatively low. The average R values for the training and test data sets at the 10-pixel scale were 0.9719 and 0.8723, respectively, and the RMSE values were 1.2222 and 3.7669, respectively. The average R values for the training and test data sets at the 20-pixel scale were 0.9779 and 0.9207, respectively, and the RMSE values were 1.0854 and 3.2778, respectively. The average R values for training and test data sets at the 30-pixel scale were 0.9778 and 0.9296, respectively, and the RMSE values were 1.0957 and 3.0965, respectively.

The simulation accuracy with three feature combination schemes at different scales and with different machine learning algorithms could be ranked as follows: scheme 1 > scheme 2 > scheme 3. The average R values of the training and test data sets in scheme 1 with different scales and algorithms were 0.9758 and 0.9265, respectively; the RMSE values

were 1.1344 and 3.3524, respectively. The average R values for the training and test data sets of scheme 2 were 0.9755 and 0.9247, respectively, while the RMSE values were 1.1397 and 3.3845, respectively. The average R values for the training and test data sets of scheme 3 were 0.9763 and 0.8990, respectively, while the RMSE values were 1.1292 and 3.4042, respectively. These outcomes suggest that introducing more characteristic parameters with a low correlation will reduce simulation accuracy.

Specific to a single test, the ET model achieved the highest accuracy in all simulation tests under the feature combination of scheme 2 at the 20-pixel scale, yielding R and RMSE values for the test set of 0.9419 and 3.0968, respectively. The sum of R of the training and test data set was the largest, while the sum of RMSE was the smallest in all tests (see Figure 3 for the simulation accuracy effect diagram). Therefore, the outcomes identified the ET model with 16 RSFs at 20-pixel scales as the optimal UAV multi-spectral LCC inversion algorithm.

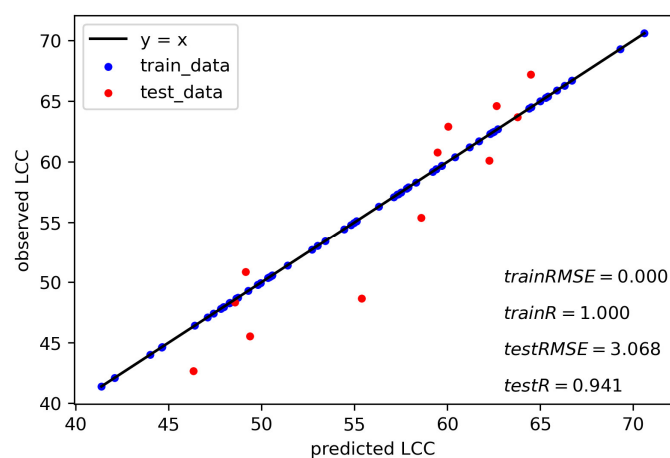


Figure 3. LCC simulation accuracy diagram of ET with UAV multi-spectral camera.

3.3. Correlation Analysis between RSFs of Sentinel-2 and LCC

The LCC inversion results for the UAV were resampled to 10 m spatial resolution via the pixel aggregation method. The LCC value of vegetation pixels in the experimental sample area and the surface reflectivity of Sentinel-2 in 12 bands were extracted correspondingly, with four edge directions truncated by 50 m and NDVI > 0.3 as the criteria to insure vegetation pixels. Finally, 8988 groups of valid data were obtained, and each VI was calculated. As RECI used the red-edge band in the vegetation index, the central wavelength of the red-edge camera's red-edge band was at 717 nm, while Sentinel-2 had two of the red-edge bands with central wavelengths at 705 nm and 740 nm; therefore, RECI was constructed with the two bands. Because 705 nm and 740 nm are located in the fifth and sixth band of Sentinel-2, they are named RECI05 and RECI06, respectively. See Table 4 for the correlation coefficients between the RSFs of Sentinel-2 and LCC. From the table, it can be seen that all features except B09 were extremely significantly correlated with LCC, and the reflectance of all bands was negatively correlated with LCC, while all VIs were positively correlated.

3.4. Sentinel-2 LCC Inversion Optimal Model

Simulations of LCC from Sentinel-2 data were conducted using two schemes with extremely significant features (11 bands reflectance in scheme 1; 11 bands reflectance and 16 VIs in scheme 2) as the input data set for the machine learning model, with 85% of the data as training data sets and 15% as test data sets. The R and RMSE of the observed and simulated values of the two data sets are listed in Table 5.

Table 4. Correlation coefficient between Sentinel-2 remote sensing features and LCC.

RS Features	R	RS Features	R	RS Features	R	RS Features	R
B01	−0.1321 **	B08	−0.0283 **	GCI	0.2548 **	NLI	0.1752 **
B02	−0.2719 **	B8A	−0.0283 **	GNDVI	0.2465 **	OSAVI	0.2333 **
B03	−0.4577 **	B09	−0.0085	MNLI	0.1538 **	RDVI	0.1915 **
B04	−0.4155 **	B11	−0.1881 **	MSAVI	0.1933 **	RECI05	0.2447 **
B05	−0.4292 **	B12	−0.1288 **	MSR	0.2611 **	RECI06	0.1959 **
B06	−0.1795 **	DVI	0.1293 **	MTVI	0.2032 **	RVI	0.2574 **
B07	−0.0307 **	EVI	0.1964 **	NDVI	0.2635 **	SAVI	0.1993 **

Note: B01, B02, B03, B04, B05, B06, B07, B08, B8A, B09, B10, and B11 represent the reflectance of Sentinel-2 in 12 bands; ** stands for $p < 0.01$.

Table 5. Summary of LCC simulation accuracy with Sentinel-2.

Regression Algorithm	Accuracy Factor	Scheme 1	Scheme 2	Regression Algorithm	Accuracy Factor	Scheme 1	Scheme 2
AB	Training R	0.5484	0.5401	GB	Training R	0.7738	0.7536
	TrainingRMSE	2.5960	2.1726		TrainingRMSE	1.5383	1.5907
	Test R	0.5214	0.5228		Test R	0.6731	0.6445
	Test RMSE	2.6145	2.2452		Test RMSE	1.8413	1.8964
ET	Training R	1.0000	1.0000	RF	Training R	0.5401	0.5386
	Training MSE	0.0000	0.0000		Training MSE	2.0217	2.0231
	Test R	0.7213	0.6704		Test R	0.5575	0.5572
	Test RMSE	1.7198	1.8397		Test RMSE	2.0804	2.0804

The accuracy analysis of the LCC simulation with Sentinel-2 data revealed that the ET model remained the best machine learning algorithm. The R value of the training set was 1.0; the RMSE was 0.0 for both schemes. Meanwhile, the R values of the test data set were 0.7213 and 0.6704 in scheme 1 and scheme 2, respectively, while the RMSE values were 1.7198 and 1.8397, respectively. The simulation accuracy of the GB model was second only to that of the ET model. Specifically, the R value of the training set was above 0.75, while the RMSE value was below 1.9; meanwhile, the R value of the test set was the lowest at 0.6445, while the RMSE was the largest at 1.8964. The simulation accuracy of the RF model ranked third overall, with the lowest R values for the training set and test set being 0.5386 and 0.5572, respectively, while the highest RMSE values were 2.0231 and 2.0804, respectively. Lastly, the overall accuracy of the AB model was the lowest among the four models. The maximum R values for the training set and test set were 0.5484 and 0.5228, respectively, while the minimum RMSE values were 2.1726 and 2.2452, respectively. Compared with the RF model, the AB model demonstrated higher precision in the training set but lower precision in the testing set.

Compared with the two feature parameterization schemes, with the exception of the AB model, the accuracy of scheme 1 was higher than that of scheme 2 in the other three models. In the ET model, the highest simulation accuracy was demonstrated in all simulations under scheme 1, with R and RMSE values for the test set of 0.7213 and 1.7198, respectively. The sum of R of the training and test data sets was the largest in all tests, while the sum of RMSE was the smallest (see Figure 4 for the simulation accuracy effect diagram). Therefore, the ET model with 11 RSFs was selected as the optimal inversion model of Sentinel-2 LCC in this study.

3.5. Regional LCC Inversion Results

Four days (1 July, 21 July, 5 August, and 4 September) in 2022 of Sentinel-2 images with little cloud cover were downloaded during the whole growth period of summer maize in Hebi City, Henan Province, China. The LCC inversion results of 4 days with cultivated land and cloud cover in Sentinel-2 SCL data set as a mask were illustrated in Figure 5.

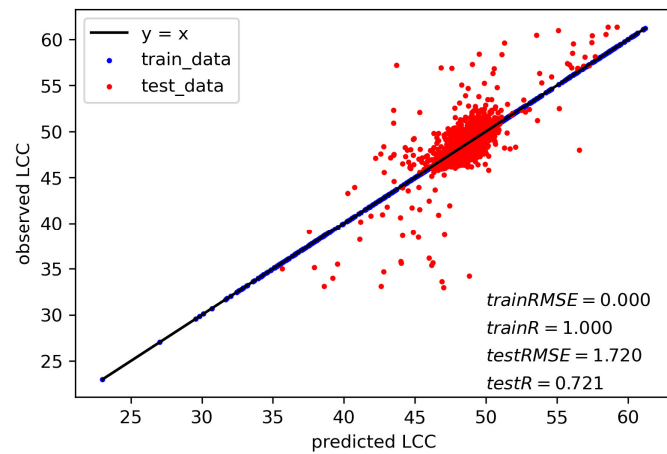


Figure 4. LCC simulation accuracy diagram of ET with Sentinel-2.

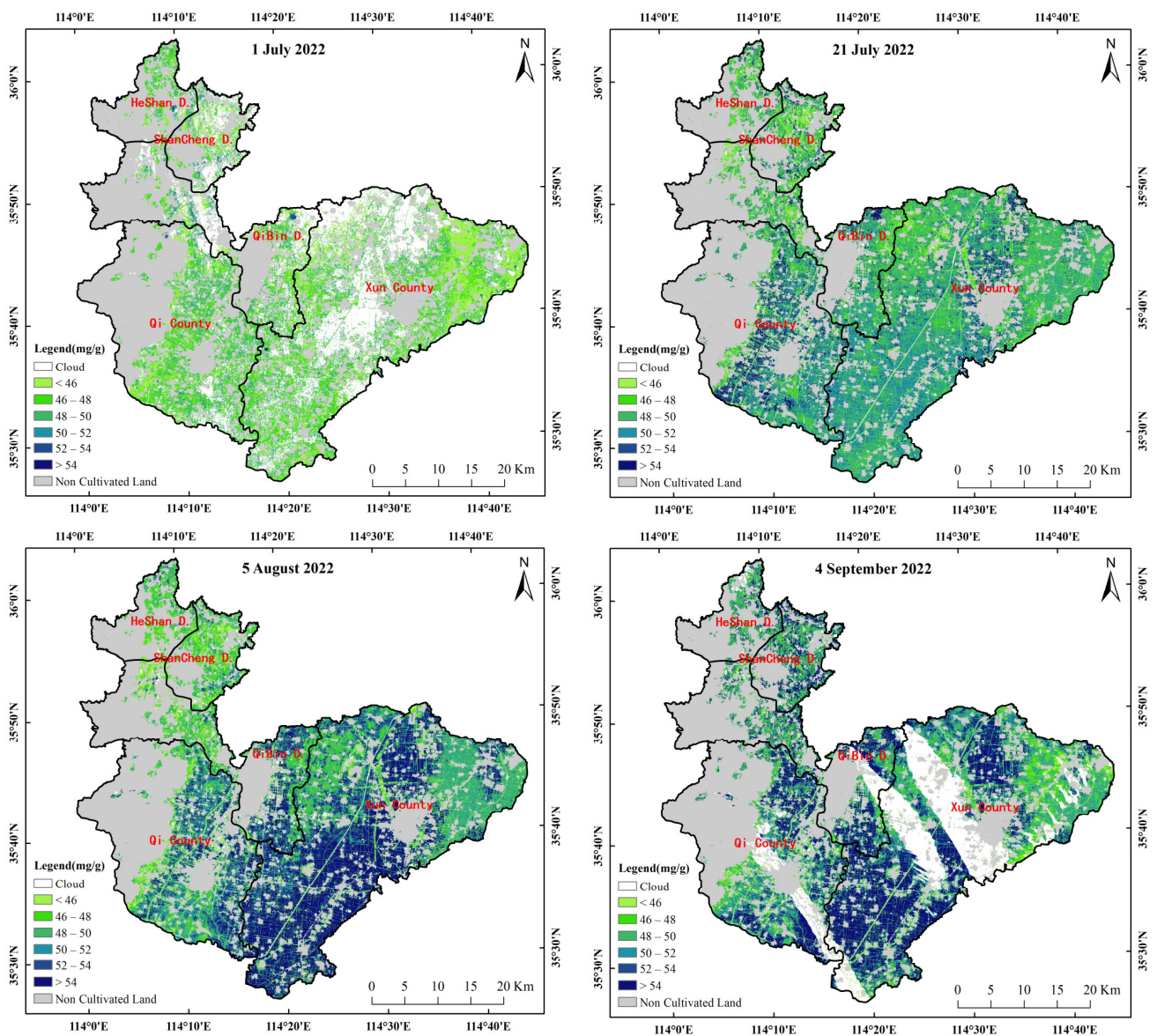


Figure 5. LCC remote sensing monitoring map of summer maize in Hebi City.

The monitoring results reveal that on 1 July, there were broken clouds distributed in central and north part of Hebi City. The average LCC of cultivated land without cloud affected was 47.3 mg/g. The average of the five districts and counties are HeShan D. 47.5 mg/g, ShanCheng D. 47.3 mg/g, QiBin D. 47.6 mg/g, Xun County 46.9 mg/g, and Qi County 47.5 mg/g. The Sentinel-2 imagery was clear sky all over the research area on 21 July, and the average LCC value of cultivated land was 49.5 mg/g. The average of the five districts and counties are HeShan D. 48.8 mg/g, ShanCheng D. 48.3 mg/g, QiBin D. 48.8 mg/g, Xun County 49.3 mg/g, and Qi County 49.8 mg/g. The average LCC value of cultivated land on 5 August was 49.8 mg/g. The average of the five districts and counties are HeShan D. 47.9 mg/g, ShanCheng D. 47.4 mg/g, QiBin D. 48.9 mg/g, Xun County 51.0 mg/g, and Qi County 49.0 mg/g. There were three obvious areas covered by cloud on 4 September, and the average LCC of cultivated land without cloud affected was 50.1 mg/g. The average of the five districts and counties are HeShan D. 50.1 mg/g, ShanCheng D. 50.4 mg/g, QiBin D. 50.5 mg/g, Xun County 49.9 mg/g, and Qi County 50.1 mg/g.

The temporal variation of LCC in Hebi City shows an increasing trend with the growth of summer maize. But LCC in the western part of the research area showed a slight decrease from 21 July to 5 August, which was probably caused by the distribution of mixed pixels with cultivated land and shrub. The spatial distribution of LCC showed a higher value in the central part while a lower value in the east and west part of the research area, while the west part was distributed with much shrub land cover and the east part with many peanuts cultivated.

4. Discussion

As a hot topic in research in recent years, UAV remote sensing has attracted extensive attention from scholars around the globe. Many scholars have carried out simulation studies on leaf area index, LCC, nitrogen content, biomass, and yield of winter wheat, but studies focused on summer maize have remained limited for various reasons. For example, the status of winter wheat in terms of China's food security is higher than that of summer corn, making research on winter wheat more meaningful. Furthermore, the high canopy of summer maize makes it difficult to carry out ground sampling observations. In addition, the multi-spectral and hyperspectral flight observations of UAVs needs relatively stable sunny weather. In the spring season, winter wheat is in the late growth period, with more sunny weather and more stability. In contrast, the growth period of summer maize is concentrated in summer, which is characterized by changeable weather, cloud coverage, and even local broken clouds, which severely reduces the quality of flight data.

This study carried out two experiments at the jointing stage and heading stage of summer maize; therefore, the applicability of the selected model in other development stages needs further study. The second experiment was affected by continuous rainy days before and after the experiment date; consequently, no suitable high-resolution earth observation satellite data were found, and the inversion results could not be upscaled to the regional scale. The experimental quadrat crops in this study were all summer maize. In 2021, the sown area of summer maize in Hebi City was 78.21 thousand hectares, accounting for 97% percent of autumn harvest grain crops [45]. The land use/land cover data released by ESRI Company in 2021 revealed that the cultivated area of the whole city was 122.9 thousand hectares (Figure 6), indicating a certain proportion of non-summer maize-cultivated land pixels in Hebi City. There were more peanut and summer maize cultivated in the eastern part of the research area according to our investigation, which caused lower monitored LCC than the central part. The applicability of the model established in this study therefore needs further verification for other crops.

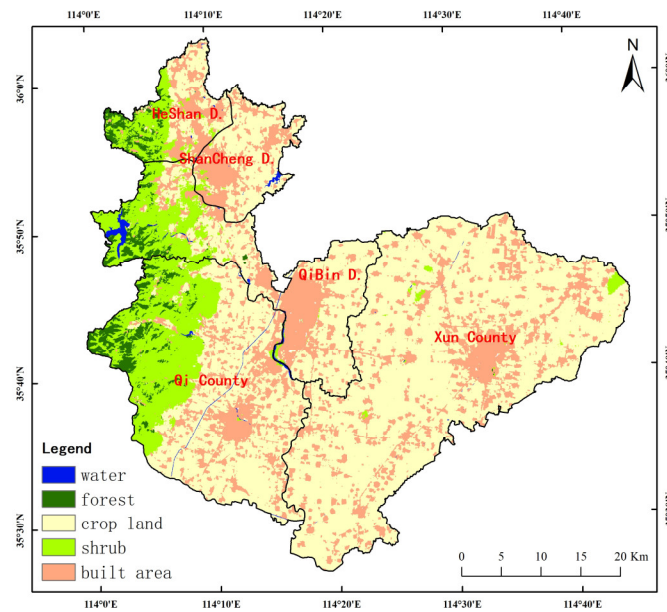


Figure 6. Land Use/Land Cover in Hebi City.

Previous research has revealed that simulation accuracy may be varied in different growth stages of crops; a study on wheat LCC monitoring after the heading stage shows partial least squares performed best at 7 and 14 days after heading, while random forest performed best at 21 days after heading [46]. The introduction of multi-source data (ground hyperspectral data, UAV visible-light data, and environment temperature data, etc.) [47] and texture indices can obviously improve simulation accuracy of LCC [48]. But in the comparison of different machine learning algorithms, different researchers may find different optimal models for LCC inversion under different conditions. Songtao Ban et al. found that partial least squares perform better than support vector machines and artificial neural networks for rice LCC monitoring in application in different regions and cultivars, with validation data set R^2 range from 0.76 to 0.81 and RMSE range from 2.24 to 4.00 in different places [49]. Random forest performs the best when multi-source data were introduced in wheat LCC monitoring, with R^2 and RMSE of test data set reach 0.7767 and 2.8387, respectively [47]. In this manuscript, the optimal algorithm and scheme for UAV LCC inversion is the ET model with the combination of 16 features at the 20-pixel scale, the R^2 and RMSE of the test data set reach 0.8872 and 3.0968, respectively, similar to previous research. For regional satellite monitoring, the ET model with 11 features performs the best, with the R^2 and RMSE for the test data set being 0.5203 and 1.7198, respectively.

In the next step, the research team will continue to carry out flight observation experiments. The test sample will cover more crop species, and the sampling time will include more growth stages to verify and further improve the research conclusions presented in this paper.

5. Conclusions

The current study explored the correlation between LCC and different remote sensing features of two kinds of multi-spectral data at different scales by testing four machine learning algorithms (AB, ET, GB, and RF) under various schemes to identify an optimal summer maize LCC remote sensing method. This exploration of the monitoring methods for the LCC of summer maize were conducted using three different scales: point ground observation, a low-altitude UAV multi-spectrum camera, and a high-resolution earth observation satellite, based on in-field simultaneous observations. The results reveal that at the scales of 10, 20, and 30 pixels, the correlation between LCC and most UAV remote sensing features increased as the scale expanded. The ET model at the 20-pixel scale with 16 characteristic parameters had the highest simulation accuracy, making it the optimal

LCC inversion model for UAV multi-spectral camera. The ET model with 11 features as input remote sensing features was the optimal model for Sentinel-2 LCC inversion. The monitored LCC from Sentinel-2 on 4 days of 2022 showed an increasing trend in the summer maize's growth stages, and the spatial distribution showed a higher value in middle part of the research area, but a lower value in east and west part.

Author Contributions: Conceptualization, L.C. and D.W.; methodology, data analysis and manuscript, H.T.; field experiment, Q.W.; review and editing, L.Z. All authors have read and agreed to the published version of the manuscript.

Funding: This research was funded by the Science and Technology Project of Henan Province (222102320035); Key Laboratory of Agrometeorological Safeguard and Applied Technique, CMA (AMF202303); Hebi Key Laboratory of Agrometeorology and Remote Sensing Anyang Observatory (AYNCOF202303).

Data Availability Statement: The data presented in this study are available from the corresponding author upon reasonable request.

Conflicts of Interest: The authors declare no conflict of interest.

References

1. Tilman, D.; Cassman, K.G.; Matson, P.A.; Naylor, R.; Polasky, S. Agricultural sustainability and intensive production practices. *Nature* **2002**, *418*, 671–677. [[CrossRef](#)] [[PubMed](#)]
2. Tremblay, N.; Bélec, C. Adapting Nitrogen Fertilization to Unpredictable Seasonal Conditions with the Least Impact on the Environment. *Horttechnology* **2006**, *16*, 408–412. [[CrossRef](#)]
3. Schröder, J.J.; Neeteson, J.J.; Oenema, O.; Struik, P.C. Does the crop or the soil indicate how to save nitrogen in maize production? Reviewing the state of the art. *Field Crop. Res.* **2000**, *66*, 151–164. [[CrossRef](#)]
4. Shanahan, J.F.; Kitchen, N.R.; Raun, W.R.; Schepers, J.S. Responsive in-season nitrogen management for cereals. *Comput. Electron. Agric.* **2008**, *61*, 51–62. [[CrossRef](#)]
5. Shiferaw, B.; Prasanna, B.M.; Hellin, J.; Bänziger, M. Crops that feed the world 6. Past successes and future challenges to the role played by maize in global food security. *Food Secur.* **2011**, *3*, 307. [[CrossRef](#)]
6. Michez, A.; Bauwens, S.; Brostaux, Y.; Hiel, M.-P.; Garré, S.; Lejeune, P.; Dumont, B. How Far Can Consumer-Grade UAV RGB Imagery Describe Crop Production? A 3D and Multitemporal Modeling Approach Applied to *Zea mays*. *Remote Sens.* **2018**, *10*, 1798. [[CrossRef](#)]
7. Longchamps, L.; Khosla, R. Precision maize cultivation techniques. In *Burleigh Dodds Series in Agricultural Science*; CGIAR Maize Research Program Manager, C.M., Watson, D., Eds.; Burleigh Dodds Science Publishing Limited: Cambridge, UK, 2017; pp. 107–148.
8. Tischler, Y.K.; Thiessen, E.; Hartung, E. Early optical detection of infection with brown rust in winter wheat by Chlorophyll fluorescence excitation spectra. *Comput. Electron. Agric.* **2018**, *146*, 77–85. [[CrossRef](#)]
9. Pinardi, M.; Bresciani, M.; Villa, P.; Cazzaniga, I.; Laini, A.; Tóth, V.; Fadel, A.; Austoni, M.; Lami, A.; Giardino, C. Spatial and temporal dynamics of primary producers in shallow lakes as seen from space: Intra-annual observations from Sentinel-2A. *Limnologica* **2018**, *72*, 32–43. [[CrossRef](#)]
10. Dou, Z.; Cui, L.; Li, J.; Zhu, Y.; Gao, C.; Pan, X.; Lei, Y.; Zhang, M.; Zhao, X.; Li, W. Hyperspectral Estimation of the Chlorophyll Content in Short-Term and Long-Term Restorations of Mangrove in Quanzhou Bay Estuary, China. *Sustainability* **2018**, *10*, 1127. [[CrossRef](#)]
11. Reyes, J.F.; Correa, C.; Zúñiga, J. Reliability of different color spaces to estimate nitrogen SPAD values in maize. *Comput. Electron. Agric.* **2017**, *143*, 14–22. [[CrossRef](#)]
12. Uddling, J.; Gelang-Alfredsson, J.; Piikki, K. Evaluating the relationship between leaf Chlorophyll concentration and SPAD-502 Chlorophyll meter readings. *Photosynth Res.* **2007**, *91*, 37–46. [[CrossRef](#)]
13. Li, J.; Feng, Y.; Mou, J.; Xu, G.; Luo, Q.; Luo, K.; Huang, S.; Shi, X.; Guan, Z.; Ye, Y.; et al. Construction and Application Effect of the Leaf Value Model Based on SPAD Value in Rice. *Sci. Agric. Sin.* **2017**, *50*, 4714–4724.
14. Shi, X.; Cai, H. Estimation of nitrogen nutrition index of greenhouse tomato under different water and nitrogen fertilizer treatments based on leaf SPAD. *Trans. Chin. Soc. Agric. Eng.* **2018**, *34*, 116–126.
15. Jia, K.; Liang, S.; Gu, X.; Baret, F.; Wei, X.; Wang, X.; Yang, Y.; Li, Y. Fractional vegetation cover estimation algorithm for Chinese GF-1 wide field view data. *Remote Sens. Environ.* **2016**, *177*, 184–191. [[CrossRef](#)]
16. Verhoef, W.; van der Tol, C.; Middleton, E.M. Hyperspectral radiative transfer modeling to explore the combined retrieval of biophysical parameters and canopy fluorescence from FLEX—Sentinel3 tandem mission multi-sensor data. *Remote Sens. Environ.* **2018**, *204*, 942–963. [[CrossRef](#)]

17. Walker, D.A.; Daniëls, F.J.A.; Alsos, I.; Bhatt, U.S.; Breen, A.L.; Buchhorn, M.; Bültmann, H.; Druckenmiller, L.A.; Edwards, M.E.; Ehrich, D.; et al. Circumpolar Arctic vegetation: A hierarchic review and roadmap toward an internationally consistent approach to survey, archive and classify tundra plot data. *Environ. Res. Lett.* **2016**, *11*, 055005. [[CrossRef](#)]
18. Manfreda, S.; McCabe, M.F.; Miller, P.E.; Lucas, R.; Pajuelo Madrigal, V.; Mallinis, G.; Ben Dor, E.; Helman, D.; Estes, L.; Ciraolo, G.; et al. On the use of unmanned aerial systems for environmental monitoring. *Remote Sens.* **2018**, *10*, 641. [[CrossRef](#)]
19. Riihimäki, H.; Luoto, M.; Heiskanen, J. Estimating fractional cover of tundra vegetation at multiple scales using unmanned aerial systems and optical satellite data. *Remote Sens. Environ.* **2019**, *224*, 119–132. [[CrossRef](#)]
20. Croft, H.; Chen, J.M.; Zhang, Y.; Simic, A.; Noland, T.L.; Nesbitt, N.; Arabian, J. Evaluating leaf Chlorophyll content prediction from multispectral remote sensing data within a physically-based modelling framework. *Isprs J. Photogramm. Remote Sens.* **2015**, *102*, 85–95. [[CrossRef](#)]
21. Sun, J.; Shi, S.; Yang, J.; Chen, B.; Gong, W. Estimating leaf Chlorophyll status using hyperspectral lidar measurements by PROSPECT model inversion. *Remote Sens. Environ. Interdiscip. J.* **2018**, *212*, 1–7. [[CrossRef](#)]
22. Verger, A.; Baret, F.; Camacho, F. Optimal modalities for radiative transfer-neural network estimation of canopy biophysical characteristics: Evaluation over an agricultural area with CHRIS/PROBA observations. *Remote Sens. Environ.* **2011**, *115*, 415–426. [[CrossRef](#)]
23. Frampton, W.J.; Dash, J.; Watmough, G.; Milton, E.J. Evaluating the capabilities of Sentinel-2 for quantitative estimation of biophysical variables in vegetation. *ISPRS J. Photogramm.* **2013**, *82*, 83–92. [[CrossRef](#)]
24. Zheng, F.; Wang, X.; Ji, J.; Ma, H.; Cui, H.; Shi, Y.; Zhao, S. Synchronous Retrieval of LAI and Cab from UAV Remote Sensing: Development of Optimal Estimation Inversion Framework. *Agronomy* **2023**, *13*, 1119. [[CrossRef](#)]
25. Tuia, D.; Verrelst, J.; Alonso, L.; Perez-Cruz, F.; Camps-Valls, G. Multioutput Support Vector Regression for Remote Sensing Biophysical Parameter Estimation. *IEEE Geosci. Remote Sens. Lett.* **2011**, *8*, 804–808. [[CrossRef](#)]
26. Verrelst, J.; Rivera, J.P.; Gitelson, A.; Delegido, J.; Moreno, J.; Camps-Valls, G. Spectral band selection for vegetation properties retrieval using Gaussian processes regression. *Int. J. Appl. Earth Obs. Geoinf.* **2016**, *52*, 554–567. [[CrossRef](#)]
27. Yang, L.; Jia, K.; Liang, S.; Wei, X.; Yao, Y.; Zhang, X. A Robust Algorithm for Estimating Surface Fractional Vegetation Cover from Landsat Data. *Remote Sens.* **2017**, *9*, 857. [[CrossRef](#)]
28. Shah, S.H.; Angel, Y.; Houborg, R.; Ali, S.; McCabe, M.F. A Random Forest Machine Learning Approach for the Retrieval of Leaf Chlorophyll Content in Wheat. *Remote Sens.* **2019**, *11*, 920. [[CrossRef](#)]
29. Kumar, C.; Mubvumba, P.; Huang, Y.; Dhillon, J.; Reddy, K. Multi-Stage Corn Yield Prediction Using High-Resolution UAV Multispectral Data and Machine Learning Models. *Agronomy* **2023**, *13*, 1277. [[CrossRef](#)]
30. Zhang, S.M.; Zhao, G.X.; Lang, K.; Su, B.W.; Chen, X.N.; Xi, X.; Zhang, H.B. Integrated Satellite, Unmanned Aerial Vehicle (UAV) and Ground Inversion of the SPAD of Winter Wheat in the Reviving Stage. *Sensors* **2019**, *19*, 1485. [[CrossRef](#)]
31. Hu, X.; Niu, B.B.; Li, X.J.; Min, X.Y. Unmanned aerial vehicle (UAV) remote sensing estimation of wheat Chlorophyll in subsidence area of coal mine with high phreatic level. *Earth Sci. Inform.* **2021**, *14*, 2171–2181. [[CrossRef](#)]
32. Lou, P.; Fu, B.; He, H.; Chen, J.; Wu, T.H.; Lin, X.C.; Liu, L.L.; Fan, D.L.; Deng, T.D. An Effective Method for Canopy Chlorophyll Content Estimation of Marsh Vegetation Based on Multi-scale Remote Sensing Data. *IEEE J. Sel. Top. Appl. Earth Obs. Remote Sens.* **2021**, *99*, 1.
33. Zhou, X.; Zhang, J.; Chen, D.; Huang, Y.; Kong, W.; Yuan, L.; Ye, H.; Huang, W. Assessment of Leaf Chlorophyll Content Models for Winter Wheat Using Landsat-8 Multispectral Remote Sensing Data. *Remote Sens.* **2020**, *12*, 2574. [[CrossRef](#)]
34. Karra, K.; Kontgis, C.; Statman-Weil, Z.; Mazzariello, J.C.; Mathis, M.; Brumby, S.P. Global Land Use/Land Cover with Sentinel-2 and Deep Learning. In Proceedings of the IGARSS 2021–2021 IEEE International Geoscience and Remote Sensing Symposium, Brussels, Belgium, 1–16 July 2021.
35. Liu, M.; Feng, R.; Ji, R.; Wu, J.; Wang, H.; Yu, W. Estimation of Leaf Area Index and Above-Ground Biomass of Spring Maize based on MODIS-NDVI. *Chin. Agric. Sci. Bull.* **2015**, *31*, 80–87.
36. Wang, Z.; Liu, C. HUETE, A Research Progress of Vegetation Index: From AVHRR-NDVI to MODIS-EVI. *J. Ecol.* **2003**, *23*, 979–987.
37. Guo, N. Vegetation Index and its Research Progress. *Drought Meteorol.* **2003**, *21*, 71–75.
38. Jia, X.; Feng, M.; Yang, W.; Wang, C. Hyperspectral Estimation of Above Ground Biomass of Winter Wheat based on Multi-Vegetation Index Combination. *J. Ecol.* **2018**, *37*, 424–429.
39. Liu, T.; Huan, Z.; Wang, Z.; He, C.; Zhang, Q.; Jiao, Y. Estimation of Leaf Area Index and Chlorophyll Content of Winter Wheat by Multi-spectrum of Unmanned Aerial Vehicle. *J. Agric. Eng.* **2021**, *37*, 65–72.
40. Pedregosa, F.; Varoquaux, G.; Gramfort, A.; Michel, V.; Thirion, B.; Grisel, O.; Blondel, M.; Prettenhofer, P.; Weiss, R.; Dubourg, V.; et al. Scikit-learn: Machine Learning in Python. *J. Mach. Learn. Res.* **2011**, *12*, 2825–2830.
41. Drucker, H. *Improving Regressors Using Boosting Techniques*; Morgan Kaufmann Publishers Inc.: Burlington, MA, USA, 1997.
42. Geurts, P.; Ernst, D.; Wehenkel, L. Extremely randomized trees. *Mach. Learn.* **2006**, *63*, 3–42. [[CrossRef](#)]
43. Friedman, J.H. Greedy Function Approximation: A Gradient Boosting Machine. *Ann. Stat.* **2001**, *29*, 1189–1232. [[CrossRef](#)]
44. Leo, B. Random Forests. *Mach. Learn.* **2001**, *45*, 5–32.
45. National Bureau of Statistics Henan Survey Corps. *Henan Survey Yearbook 2022*; China Statistics Publishing House: Beijing, China, 2022.
46. Wu, Q.; Zhang, Y.; Zhao, Z.; Xie, M.; Hou, D. Estimation of Relative Chlorophyll Content in Spring Wheat Based on Multi-Temporal UAV Remote Sensing. *Agronomy* **2023**, *13*, 211. [[CrossRef](#)]

47. Zhao, J.; Pan, F.; Xiao, X.; Hu, L.; Wang, X.; Yan, Y.; Zhang, S.; Tian, B.; Yu, H.; Lan, Y. Summer Maize Growth Estimation Based on Near-Surface Multi-Source Data. *Agronomy* **2023**, *13*, 532. [[CrossRef](#)]
48. Wang, Y.; Tan, S.; Jia, X.; Qi, L.; Liu, S.; Lu, H.; Wang, C.; Liu, W.; Zhao, X.; He, L.; et al. Estimating Relative Chlorophyll Content in Rice Leaves Using Unmanned Aerial Vehicle Multi-Spectral Images and Spectral–Textural Analysis. *Agronomy* **2023**, *13*, 1541. [[CrossRef](#)]
49. Ban, S.; Liu, W.; Tian, M.; Wang, Q.; Yuan, T.; Chang, Q.; Li, L. Rice Leaf Chlorophyll Content Estimation Using UAV-Based Spectral Images in Different Regions. *Agronomy* **2022**, *12*, 2832. [[CrossRef](#)]

Disclaimer/Publisher’s Note: The statements, opinions and data contained in all publications are solely those of the individual author(s) and contributor(s) and not of MDPI and/or the editor(s). MDPI and/or the editor(s) disclaim responsibility for any injury to people or property resulting from any ideas, methods, instructions or products referred to in the content.